Journal of Magnetism and Magnetic Materials 402 (2016) 34–43

Contents lists available at ScienceDirect

Journal of Magnetism and Magnetic Materials

journal homepage: www.elsevier.com/locate/jmmm

Synthesis, characterization, and cytotoxicity of the plasmid EGFP-p53 loaded on pullulan–spermine magnetic nanoparticles

Touba Eslaminejad [a], Seyed Noureddin Nematollahi-Mahani [b,c,d], Mehdi Ansari [a,e,*]

[a] Pharmaceutics Research Centre, Institute of Neuropharmacology, Kerman University of Medical Sciences, Kerman, Iran
[b] Department of Anatomy, Afzalipour School of Medicine, Kerman University of Medical Sciences, Kerman, Iran
[c] Neuroscience Research Centre, Institute of Neuropharmacology, Kerman University of Medical Sciences, Kerman, Iran
[d] Afzal Research Institute, Kerman, Iran
[e] Pharmaceutics Research Centre, Faculty of Pharmacy, Kerman University of Medical Sciences, Kerman, Iran

ARTICLE INFO

Article history:
Received 2 September 2015
Received in revised form
8 November 2015
Accepted 11 November 2015
Available online 14 November 2015

Keywords:
Magnetic nanoparticles
Pullulan
Spermine
Targeting
Cytotoxicity
Gene delivery

ABSTRACT

Magnetic nanoparticles have been used as effective vehicles for the targeted delivery of therapeutic agents that can be controlled in their concentration and distribution to a desired part of the body by using externally driven magnets. This study focuses on the synthesis, characterization, and functionalization of pullulan–spermine (PS) magnetic nanoparticles for medical applications. Magnetite nanopowder was produced by thermal decomposition of goethite (FeOOH) in oleic acid and 1-octadecene; pullulan–spermine was deposited on the magnetite nanoparticles in the form of pullulan–spermine clusters. EGFP-p53 plasmid was loaded on functionalized iron oleate to transfer into cells. Synthesized nanoparticles were characterized by Fourier transform infrared spectroscopy (FTIR), dynamic light scattering (DLS), vibrating sample magnetometry (VSM), and transmission electron microscopy (TEM). The encapsulation efficiency and drug loading efficiency of the nanocomplexes were tested. FTIR studies showed the presence of oleic acid and 1-octadecene in the iron oleate nanopowder and verified the interaction between spermine and pullulan. The characteristic bands of PS in the spectrum of the pullulan–spermine-coated iron oleate (PSCFO) confirmed that PS covered the surface of the iron oleate particles. TEM studies showed the average size of the iron oleate nanopowder, the PSCFO, and the plasmid-carrying PSCFO (PSCFO/pEGFP-p53) to be 34 ± 12 nm, 100 ± 50 nm and 172 ± 3 nm, respectively. Magnetic measurements revealed that magnetic saturation of the PSCFO was lower in comparison with the iron oleate nanopowder due to the presence of organic compounds in the former. In cytotoxicity tests performed using U87 cells as glioblastoma cells, a 92% survival rate was observed at 50 μg/μl of the plasmid-carrying PSCFO, with an IC_{50} value of 189 μg/μl.

1. Introduction

Cancer is commonly treated with a combination of surgery, radiation therapy, chemotherapy, and photodynamic therapy (PDT) [1]. While chemotherapy is an effective treatment, the side effects of its toxicity are often severe and devastating when delivered as a full body dose to the patient. Recent developments employing nanotechnology have made it possible to deliver a drug to the targeted tissue across biological barriers, and to release it at a controlled rate that minimizes cell and tissue degradation [2]. In this regard, magnetic nanoparticles have shown great potential in targeted drug delivery for cancer treatment [3]. For example, magnetic nanoparticles coated with activated carbon are able to transport pharmaceuticals to a specific site in the body when facilitated by an external magnetic field. This allows more concentrated doses of drugs to be delivered to relevant cells, and kept on site longer. Chemical and physical vapor deposition and mechanical attrition are used in the preparation of nanoparticles [4] where homogeneity, particle size and size distribution, morphology, and agglomerate size are the most important parameters in product specification [5]. The thermodynamically equilibrated state of the particles is restored by condensation of nuclei of the reaction product, and controlled by the kinetics of the nucleation and growth [6]. Kinetic factors (e.g. reaction rates, transport rates of reactants, and the removal and redistribution of matter) control

* Corresponding author at: Pharmaceutics Research Centre, Faculty of Pharmacy, Kerman University of Medical Sciences, Haft-Bagh Boulevard, PO Box 76175-439, 7616931555 Kerman, Iran.
E-mail addresses: tslaminejad@yahoo.com (T. Eslaminejad), nnematollahi@kmu.ac.ir, nematollahimahani@yahoo.com (S.N. Nematollahi-Mahani), mansari@kmu.ac.ir, mansari1345@yahoo.com (M. Ansari).

http://dx.doi.org/10.1016/j.jmmm.2015.11.037
0304-8853/

the dynamics of the thermodynamic equilibrium of the system [7]. The reaction and transport rates are affected by the temperature, pH and mixing of the reactants, as well as their respective concentrations. Particle morphology is influenced by factors such as supersaturation, colloidal stability, nucleation and growth rates, recrystallization, and aging times [8]. In particular, supersaturation has a dominant role in determining the morphology of precipitates [9]. To prevent dangerous agglomeration of the particles in the blood stream, magnetic nanoparticles must be tailor-made [10] to avoid agglomeration of particles occurring during drying, handling, and post-processing [11]. In this regard, surfactants can help control particle dispersion during chemical synthesis [12]. Another aspect requiring attention in the synthesis of nanoparticles is the annealing process which causes an increase in crystallinity, that in turn greatly affects the magnetic and electronic properties of particles [13]. Molecular weight, surface charges, amphiphilicity, as well as the structure and shape of particles, also affect the efficiency of gene transfection through polymer-based vectors [14]. While cationic polymers such as polyethyleneimine (PEI), poly L-lysine (PLL), chitosan, and polyamidoamines (PAMAM) are commonly used in gene delivery [15], pullulan–spermine complexing with plasmid DNA has been shown to be a potent carrier system for non-viral gene therapy [16]. Such complexes are known to undergo cellular endocytosis via clathrin-dependent endocytosis [17]. Pullulan is recognized by the asialoglycoprotein receptor (ASGPR) found primarily in the liver, but cells which do not express ASGPR are also able to internalize pullulan–spermine [16,18]. Oncogenes and tumor suppressor genes are the two main types of genes that play a role in cancer [19,20]. Tumor suppressor genes have been found, including TP53 (p53), BRCA1 and BRCA2 (for breast cancer), APC (colorectal tumors) and RB1 (retinoblastoma) [21]. Abnormalities of the TP53 gene have been found in more than half of human cancers [22]. The p53 protein is involved in the pathway to apoptosis and a cell with DNA damage that cannot be repaired continue to grow and divide, and then lead to cancer [23,24]. The outcomes of common cancer therapy for malignant glioblastoma are still very poor with less than 5% of patients surviving five years post diagnosis even with the best current treatment [25]. Bearing all this in mind, we hypothesized that the incorporation of magnetic nanoparticles to pullulan–spermine gene delivery nanocarriers could promote effective cellular uptake via a targeting delivery system. Hence, the main aim of this study was to develop a chemically modified magnetic nanoparticle vector for gene delivery systems to improve their targeting gene therapy. Accordingly, magnetic nanoparticles were prepared and characterized by FTIR, DLS, VSM, and TEM techniques. Their cytotoxicity in the human glioblastoma cell line U87 and their ability to protect genes from physical, chemical, and enzymatic degradation were evaluated. Finally magnetic nanoparticles were experienced against glioblastoma cell line, U87, to show their therapeutic efficacy in vitro and in vivo experiments.

2. Experimental

Goethite (FeOOH), 1-octadecene, spermine, pullulan, carbonyldiimidazole (CDI), Dulbecco's modified eagle's medium F12 (DMEM), fetal bovine serum (FBS), penicillin–streptomycin (100 μg/ml), phosphate-buffered saline (PBS), 2-(2-methoxy-4-nitrophenyl)-3-(4-nitrophenyl)-5-(2, 4-disulfophenyl)-2H-tetrazolium (WST-1 reagent), poly vinyl alcohol (PVA), and dimethyl sulphoxide (DMSO) were purchased from the Sigma Aldrich Company (Mo, USA). Dimethyl formamide (DMF) and oleic acid were obtained from the Merck Company (Darmstadt, Germany). The GeneJET Plasmid Miniprep Kit was obtained from Thermo Scientific while U87 glioblastoma cells were obtained from the Pasteur Institute of Iran.

2.1. Construction of plasmid

The construction of the pEGFP-p53 vector (5.89 kb) coding for the enhanced green fluorescent protein (EGFP), which contained the tumor protein p53 gene that acts as a tumor suppressor, was undertaken based on methods previously described [26]. The full-length 1191 bp tumor protein p53 (Tp53) gene (GenBank AAD28628.1) that encodes 397 amino acids was synthesized using a DNA synthesizer and sub-cloned into the pBR322 vector using the PstI and BamHI sites. The recombinant pBR322-p53 plasmid containing the Tp53 gene was verified by restriction enzyme digestion and sequencing. The Tp53 was then sub-cloned into the pEGFP-N1 vector, and the digested products of the recombinant plasmid were verified by agarose gel electrophoresis. Then pEGFP-p53 was propagated in an *Escherichia coli* strain Top 10 (ATCC® PTA-10989™) and purified by the GeneJET Plasmid Miniprep® Kit according to the manufacturer's protocol. Both the yield and purity of the pEGFP-p53 were evaluated by UV spectroscopy. The absorbance ratio at wavelengths of 260–280 nm for DNA solution was between 1.8 and 2.0 after dilution to between 1:500 and 1:1000 in TE buffer.

2.2. Synthesis of magnetite nanoparticles

The synthesis of magnetite nanoparticles (Fe_3O_4) basically followed the procedure reported by Colvin [27]. Magnetite nanocrystals were synthesized in a three-neck flask equipped with a condenser, magnetic stirrer, thermocouple, and heating mantle. Typically, a mixture of 0.178 g FeOOH fine powder (2.00 mmol), 2.26 g oleic acid (8.00 mmol) and 5.00 g 1-octadecene (20 mmol) was heated with stirring to 320 °C and maintained at this temperature for 1 h. On completion of the reaction, the product was allowed to cool to room temperature and 30 ml ethanol was added. The resulting black precipitate was separated by centrifugation at 6300 g for 20 min. During this time the supernatant turned from turbid black to clear brown as the iron source material dissolved and formed an iron carboxylate salt. The reaction was protected under argon in order to avoid any undesired side-reactions (e.g. oxidation of oleic acid).

2.3. Preparation of pullulan–spermine (PS)

Spermine was introduced to the hydroxyl groups of pullulan by a CDI activation method [28]. Pullulan (25 mg) was dissolved in 2.5 ml DMSO and 435 mg of CDI was then added to reach a molar ratio of 3:1 for CDI to the hydroxyl groups of pullulan. The CDI–pullulan mixture was incubated for 5 min at room temperature. Spermine (2500 mg) was dissolved in 22.5 ml DMSO was added drop-wise to reach a large molar excess of spermine in order to prevent cross linking of pullulan. The mixture was then incubated overnight at 40 °C and purified by dialysis in deionized water.

2.4. Surface functionalization of nanoparticles

Pullulan–spermine-coated iron oleate (PSCFO) was prepared by a solvent diffusion method. Wet magnetite gel (50 mg) and 100 mg of pullulan–spermine were dissolved in separate 5 ml portions of DMF and the two portions were mixed using a vortex mixer. The resulting mixture was then added to 90 ml of PVA (0.5%, w/w) by means of a syringe that was positioned with the needle directly in the medium, with moderate mechanical stirring. The magnetic particles were isolated by ultracentrifugation at 29,000g for 20 min at 4 °C and washed three times with deionized water before freeze-drying for later characterization.

2.5. Preparation of polyion complexes

To prepare polyion complex (PIC) micelles, 25 μl of PSCFO and PS (10 μg/μl in deionized water) was mixed with an equal volume of pEGFP-p53 plasmid DNA (0.1 μg/μl). The PIC composition was calculated on the basis of nitrogen number of pullulan–spermine (*N*) per phosphorus number of plasmid DNA (*P*) and expressed as the *N*/*P* ratio.

2.6. Characterization of nanoparticles

FTIR spectra of iron oleate, PS, and PSCFO were recorded as KBr discs in the range 3500–500 cm^{-1} on Bruker Optics' RockSolid™ design. The mean particle size and the size distribution of the nanoparticles were determined by photon correlation spectroscopy (PCS). The zeta potential values of the nanoparticles were obtained by laser doppler anemometry (LDA) that measured the mean electrophoretic mobility. Samples of iron oleate, PS, and PSCFO, PS/pEGFP, and PSCFO/pEGFP suspensions were diluted at the appropriate concentrations with filtered water for PCS and LDA. PCS and LDA analyses were performed with a Zetasizer® 3000 HS particle size analyzer (Malvern Instruments, UK). Light scattering measurements were made in triplicate on samples that were sufficiently diluted to prevent multiple scattering. Nanoparticle morphology, size distribution, and average particle diameter were investigated by TEM in both the secondary and the backscattered electron modes using a Zeiss EM10C transmission electron microscope operated at 80 kV accelerating voltage. For TEM studies, samples of the iron oleate, PS, PSCFO, PS/pEGFP-p53, and PSCFO/pEGFP-p53 were suspended in acetone and sonicated for 30 min. A 10 μl drop of the sample was adsorbed on to a formvar carbon coated grid Copper Mesh 300. After 5 min, excess liquid was wicked with filter paper, and the sample was loaded into the vacuum stage of the microscope and visualized. Size distribution and average particle diameter were determined analyzing 5–10 images, representing a population of more than 2000 particles. The content of iron oleate in the PSCFO was determined by using a BAHR STA 503 thermoanlyzer. Samples weighing between 5 and 15 mg were heated from 10 to 800 °C at a heating rate of 10 °C/min in air. The magnetic properties of nanoparticles were measured at room temperature (RT) using a VSM-7300 vibrating sample magnetometer (VSM) (Meghnatis Daghigh Kavir Co., Kashan, Iran) in a maximum applied field of 10 kOe. Samples were attached with a glass rod to the vibrator using Teflon coupling. The vibration was along the *z*-axis with fixed amplitude of 5 mm and frequency of 23 Hz. The magnetic field was applied along the *x*-axis by means of an electromagnet capable of producing fields up to two Tesla. The magnetic moment of the vibrating sample induced an electromotive force in the pick-up coils arranged along the *x*-axis. A standard nickel sample was used to calibrate the system. Magnetization curves for samples were used to analyze the results. From the hysteresis loops obtained, the saturation magnetization (M_s), remnant magnetization (M_r), and coercivity (H_c) were determined.

The bonding of pEGFP-p53 to PS and PSCFO was studied by agarose gel electrophoresis run for 30 min at 100 V (Sub-Cell GT 96/192, Bio-Rad Laboratories Ltd., England), followed by ethidium bromide (EtBr) staining. The capture of DNA on to the polymer was examined to evaluate its condensation ability. A blank comprising a complex of pEGFP-p53 (20 μg/ml) and EtBr (0.4 mg/ml) was used to calibrate to 100% fluorescence. The fluorescence intensity of the samples (excitation: 510 nm, emission: 590 nm) was measured 15 min later using a spectrofluorophotometer (RP-5000; Shimadzu, Japan). The results were expressed as relative fluorescence intensity (percent decrease against the pEGFP-p53-EtBr complex). Sample fluorescence was determined after subtracting the baseline fluorescence of EtBr in the absence of the DNA. The relative fluorescence was based on two independent experiments and calculated using the following Eq. (1) [29]:

$$\%\ \text{Relative Fl.} = (\text{Fl.}_{\text{Obs}} - \text{Fl.}_{\text{EtBr}}\ / \text{Fl.}_{(\text{pDNA+EtBr})} - \text{Fl.}_{\text{EtBr}}) \times 100 \quad (1)$$

where Fl._{Obs} is the fluorescence intensity of complex; Fl._{EtBr} is the fluorescence of EtBr alone; $\text{Fl.}_{(\text{pDNA+EtBr})}$ is the fluorescence of pDNA + EtBr.

To discriminate between DNA adhesion to the carrier and actual incorporation, extracellular fluorescence was examined with an Olympus TH 1400 fluorescence microscope (254 nm wavelength) which was quenched by the addition of trypan blue (0.2 mg/ml, pH 4.4) to PS/pEGFP-p53 and PSCFO /pEGFP-p53 [30], the non-quenched fraction thus representing encapsulated DNA.

2.7. Electrophoretic nuclease resistance and stability assays

To investigate the ability of the copolymer to protect DNA from enzymatic degradation, 3 μl of naked pEGFP-p53, PS/pEGFP-p53, and PSCFO/pEGFP-p53 (containing 0.75 μg plasmid) were combined with 2 U DNase I in 4 μl 50 mM Tris–HCl/10 mM $MgCl_2$ at pH 7.4. After incubation for 1 h at 37 °C, the sample was run on an agarose gel and visualized using a UV image capture system. Naked pEGFP-p53 served as a negative control. For stability assays, PS/pEGFP-p53 and PSCFO/pEGFP-p53 complexes (7%) were prepared and incubated in serum-free medium for up to 7 days. The fluorescent intensity of bands corresponding to DNA and their electrophoretic mobility were observed and compared with those obtained with naked pEGFP-p53 and PS/pEGFP-p53, and PSCFO/pEGFP-p53 complexes in the absence of serum-free medium.

2.8. In vitro release of DNA

To quantify the DNA release from the nanostructured systems, 4 mg of PS/pEGFP-p53 and PSCFO/pEGFP-p53 nanoparticles were incubated in PBS (pH 7.4, 37 °C) with gentle magnetic stirring for 72 h. Samples were centrifuged for 10 min at 16,000*g* and the supernatant was removed and replaced with fresh buffer. At fixed time points (5, 9, 18, 23, and 30 days), supernatant was collected, analyzed by spectrophotometry, and the kinetics of DNA release from samples were assessed. All measurements were carried out in triplicate.

2.9. Cell culture

Non-transformed U87 cells were maintained in DMEM supplemented with 10% FBS and 100 μg/ml penicillin/streptomycin at 37 °C; 5% CO_2.

2.10. Cytotoxicity assay

To seed cells for the cytotoxicity assay, trypsinized U87 cells were first re-suspended in the cell culture medium at a density of 2×10^5 cells/ml. After incubating the cells for 24 h, the medium was changed to a fresh serum-free medium, and 100 μl of the prepared magnetic transfection complexes of each concentration (0, 50, 75, 100, 250 and 500 μg/μl) were applied to each well of an ELISA plate. The plates were then incubated at 37 °C; 5% CO_2 for 24 h. The medium was subsequently changed to DMEM and 10 μl of WST-1 solution was added, and the cells were allowed to incubate for 3 h. The absorbance of samples was measured by an ELISA reader (BioTek® Elx 800) at 450 nm with the reference at 630 nm. Cell viability was expressed as 100% for control, non-treated cells. All samples were run in three replicates and the experiments were repeated twice. The survival rate (%) was

calculated following equation (2) [31]:

$$\% \text{ Survival rate} = (\text{OD in treatment group}/\text{OD in control group}) \times 100 \quad (2)$$

The inhibitory concentration required for 50% cytotoxicity (IC_{50}) value was determined using the Prism dose-response curve (Prism Graphpad, Prism version version 6 for windows, GraphPad Software, Sa Diego, CA, USA), and plotting the percentage of inhibition versus the concentration.

3. Results and discussion

In this study, magnetic pullulan–spermine (PS) nanoparticles were prepared and evaluated as possible carriers for therapeutic agents. A plasmid comprising the pEGFP-p53 vector containing the tumor protein p53 gene served as a model curative transported by the nanoparticles. Although the thermal decomposition method of preparing Fe_3O_4 has many advantages for producing highly monodispersed particles with a narrow size distribution, it has, nevertheless, a significant disadvantage in that the resulting particles are generally soluble only in nonpolar solvents [32].

The ratios of the starting reagents including the organometallic compounds (goethite), surfactant (oleic acid), and solvent (1-octadecence) together with the reaction temperature and reaction time are the main parameters for controlling nanoparticle synthesis. The original red color of the hematite (α-Fe_2O_3) gradually changed to brown as the reaction process proceeded and led to the disappearance of the hematite diffraction peaks. Finally, the color of the reactant changed from brown to black as a result of the decomposition of iron oleate and the formation of nanoparticles. FTIR analyses showed that the magnetite (Fe_3O_4) was completely covered by fatty acid [33].

Goethite powder is generally stable in air and is extremely cost-effective compared to their organometallic compounds [34]. The magnetic structure of the surface layer is usually different from that in the body of nanoparticle, and the magnetic interactions in the surface layer could have a notable effect on the magnetic properties of nanoparticles. Therefore, the interaction between the surfactant and the nanoparticle is critical to synthesis and application of nanoparticles. Oleic acid is known to provide a good protective surfactant for oxide-based nanoparticles [35]. It is used to stabilize the magnetic nanoparticles with strong chemical bonding between the carboxylic acid and the amorphous iron oxide nanoparticles. In this regard, oleic acid as a biologically safe molecule covered the surface of the Fe_3O_4 to control their particle size, prevent aggregation, achieve biocompatibility, and increase lipophilicity and stability [36]. Recently, black copolymers have been used for the formation of shells for encapsulation of nanoparticles. They promote particle interaction, solubility, and potentially a uniform shape of the core shell nanoparticles. The hydrophobic chains of the octadecence magnetic block are able to interpenetrate the surface-bound oleic acid ligands. X-ray analysis show that 99.9% of the polymeric shells contain only a single nanoparticle [37]. However, the naked iron oxide nanoparticles have high chemical activity, and are easily oxidized in air, resulting in the loss of magnetism and dispersibility. Therefore, it is very important to provide a proper surface coating and deploy effective protection strategies to maintain the stability of magnetic iron oxide particles. In our studies, surfactants, polymers, and biomolecules, etc. were used for functionalization.

3.1. FTIR spectra

Fig. 1(a) shows infrared spectra of magnetic particles covered with oleic acid. The absorption bands in region from 400 cm^{-1} to 600 cm^{-1} correspond to goethite. The presence of oleic acid is obvious in the sample. The absorption bands at 2341 and 2360 cm^{-1} refer to the CH_2 groups in oleic acid and 1-octadecene. Another band can be observed at 1632 cm^{-1}, which has been shifted left from 1710 cm^{-1} (C=O bond asymmetric vibration). This can be attributed to the carboxyl groups of oleic acid combining with the iron atoms on the surface of iron oleate nanoparticles. This renders a partial single bond character of the C=O bond that weakens it and shifts the stretching frequency to a lower value. Carboxyl groups of oleic acid are chemisorbed to the surface. FTIR spectra of PS (Fig. 1(b)) confirm the introduction of spermine into pullulan, as indicated by the C=O stretch at

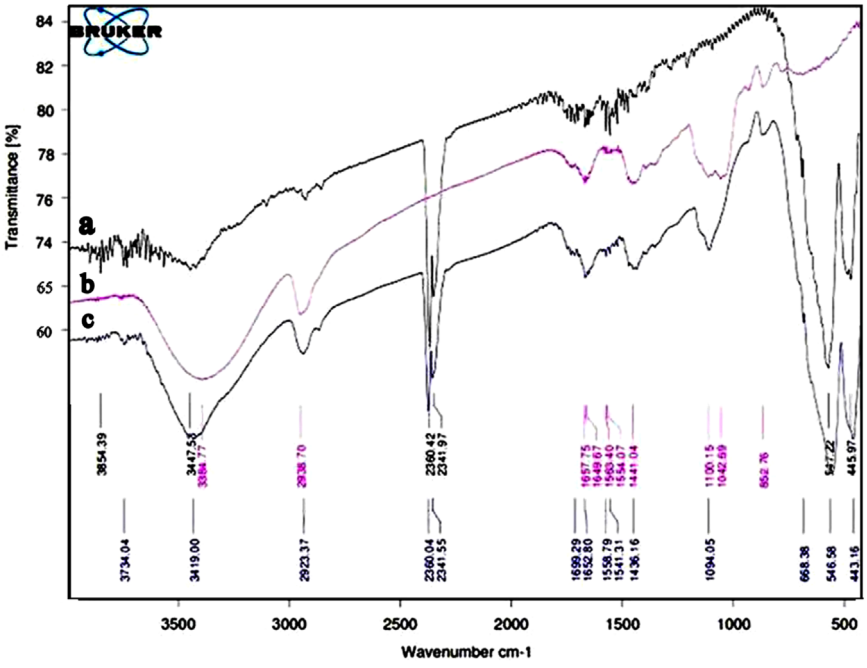

Fig. 1. FTIR spectra of iron oleate (a), PS (b) and PSCFO (c).

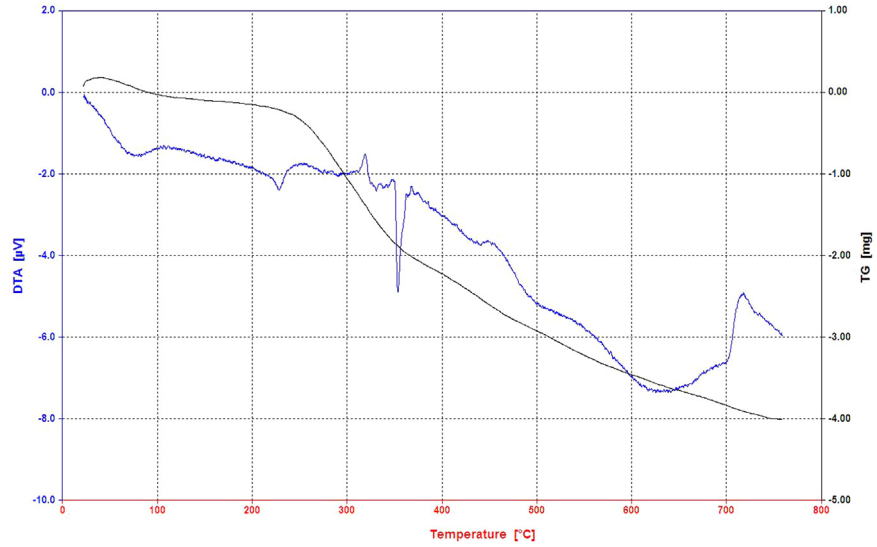

Fig. 2. TGA (black) and DTGA (blue) thermograms of iron oleate and PSCFO nanoparticles. (For interpretation of the references to color in this figure legend, the reader is referred to the web version of this article.)

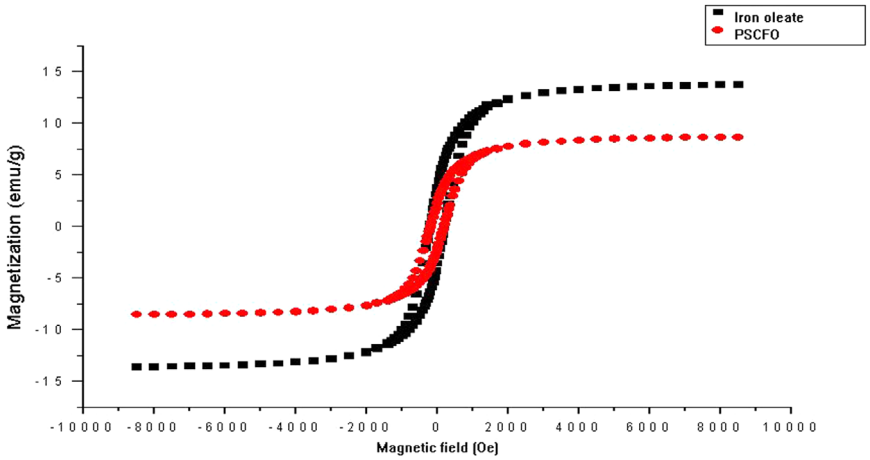

Fig. 3. Magnetization curves of naked iron oleate and PSCFO.

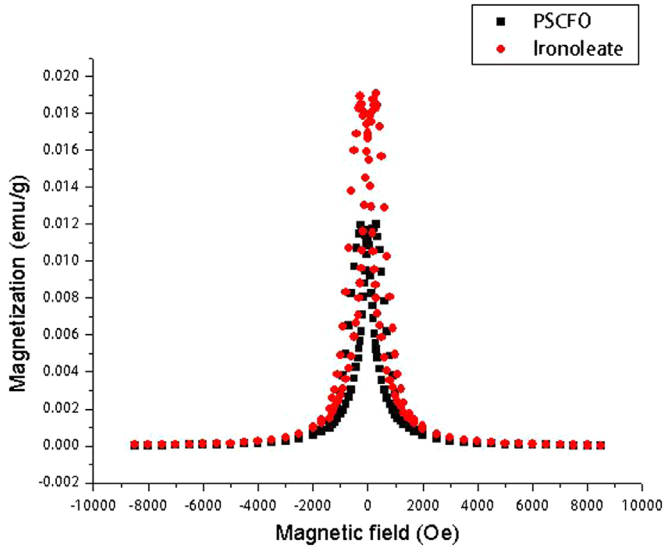

Fig. 4. Magnetization vs. applied magnetic field for naked iron oleate and PSCFO.

1657 cm^{-1}, O–C=O bend at 1441 cm^{-1}, and CH_3 deformation at 1100 cm^{-1} and N–H bend at 852 cm^{-1}. The absorption bands at 2939 cm^{-1} are the strong CH_2 bands characteristic of CH_2 groups that are present in pullulan and spermine. The absorption peak at 3384 cm^{-1} arising from the stretching vibration of the hydroxyl group is weaker in the spectrum of PS as compared to that in pullulan. Comparing the FTIR spectra of iron oleate (Fig. 1(a)) and that of PSCFO (Fig. 1(c)), the characteristic bands of PS appearing near 2923, 1652, 1558, 1541, 1436 and 1094 cm^{-1} in the spectrum of the PSCFO confirm that PS covered the surface of the nanoparticles.

It can be seen that the intensity of the C–O stretching at 1709 cm^{-1} is significantly reduced in the iron oleate, and a new peak centered at 1551 cm^{-1} is formed. This result is consistent with the formation of iron carboxylate bonds in the Fe_3O_4. The iron oleate spectrum also shows evidence of vinyl C–H stretching at 2341 cm^{-1} and 2360 cm^{-1}, indicating that the oleate ligand does not transform to stearate during the synthesis process. Finally, the broad band at 400–600 cm^{-1} is attributed to a stretching of the Fe–O bonds. Iron carboxylates tend to form Fe_3 (μ_3-O) clusters which show one Fe–O stretching band in the $Fe_3^{III}O$ and two Fe–O bands in the mixed-valence $Fe_2^{III}Fe^{II}O$. The results obtained in this study are consistent with those reported by [38].

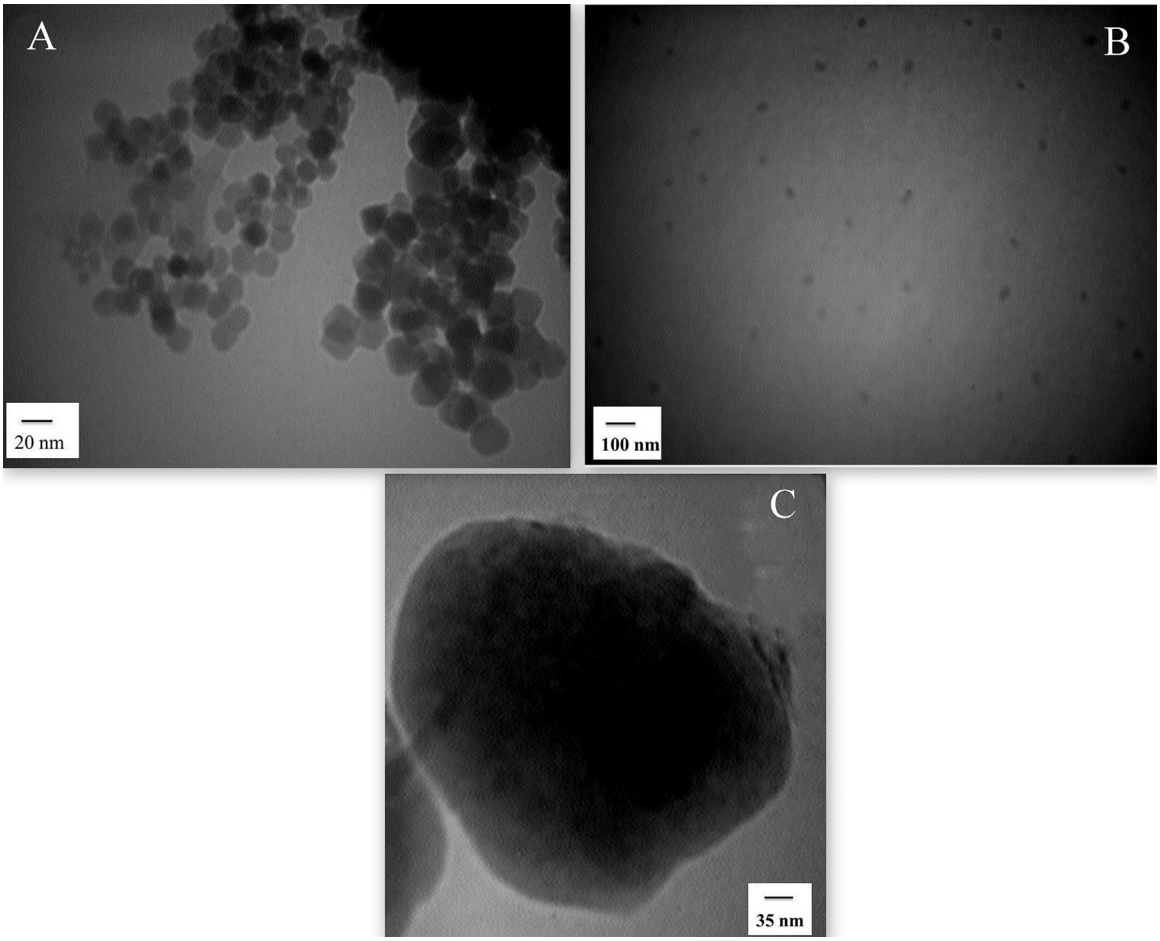

Fig. 5. TEM micrographs of nanoparticles prepared by thermal decomposition method. Iron oleate before functionalization (A), iron oleate after functionalization by PS in two magnifications 100, 35 nm (B and C).

3.2. Simultaneous thermal analysis

TGA and DTGA of iron oleate and PSCFO nanocomposites are shown in Fig. 2. The thermogram of iron oleate and PSCFO shows that the initial decomposition stage in the temperature range from 50 to 150 °C represents the water evolving (mass loss 8%). The second decomposition event in the temperature range of 250–350 °C with mass loss of 40% corresponds to the organic breakdown of PS polysaccharide chains, with total mass loss of up to 80% at 700 °C. Therefore, an estimate from the TGA curve estimates the content of the Fe_3O_4 in the PSCFO to be about 20%. The DTGA graph shows a peak at about 230 °C, and three to four peaks in the range of 300–400 °C. Releasing of water began at about 40 °C and continued to 200 °C, and from about 200–500 °C, the organic constituent in the organically modified layers began to decompose.

3.3. Magnetic properties

Magnetization curves (M–H loop) for the iron oleate and PSCFO measured at RT are presented in Fig. 3. At the maximum applied magnetic field of 10 KOe, the magnetization did not reach saturation and no hysteresis loops could be observed (no remanent magnetization and zero coercivity fields) [38]. The results indicated that the iron oleate and PSCFO were superparamagnetic at RT, with a calculated M_s of 14 and 9 emu/g respectively [39]. The hysteresis loop analysis of the iron oleate and PSCFO at RT can be used to confirm the average size and particle size distribution of iron oleate and PSCFO already obtained from DLS and TEM analyses. The decrease in saturation is ascribed to the size effect. The magnetic particle size and size distribution could also be calculated from the hysteresis curve using the following Eq. (3) [39]:

$$D_m = \left((18K_B T/\pi)(X_i/\rho M_s) \right)^{1/3} \quad (3)$$

where X_i is the initial magnetic susceptibility, $X_i = (dM/dH)_{H\to 0}$ which mainly arises from the largest particles, M is (mass) magnetization of particles, and H is magnetic field strength, magnetizing force. ρ is the density of iron oleate (5.18 g/cm^3), and K_B is Boltzmann constant.

The initial slope near the origin was determined from the hysteresis plots by curve-fitting the linear portion of the data. Thus, the magnetic particle size, D_m, of samples was estimated to be 9.4 and 10 nm for iron oleate and PSCFO, respectively. For superparamagnetic particles, the true magnetic moment (μ) at a particular temperature can be calculated using the Langevin equation (4) [40]:

$$M = M_s\left(\coth(\mu H/K_B T) - K_B T/\mu H \right) \quad (4)$$

where $\mu = M_s \pi D^3/6$ is the true magnetic moment of each particle, D the diameter of the particle, K_B the Boltzmann constant, T the absolute temperature (300 °K), and M_s is the saturation magnetization. Fig. 4 shows the best fit for the Langevin Eq. (4). From this data fit, the mean-magnetic moment per particle of sample was found to be near two μ_B. Results show that the particles have typical superparamagnetic characteristics.

The M_S value for the PSCFO was lower than that of the naked

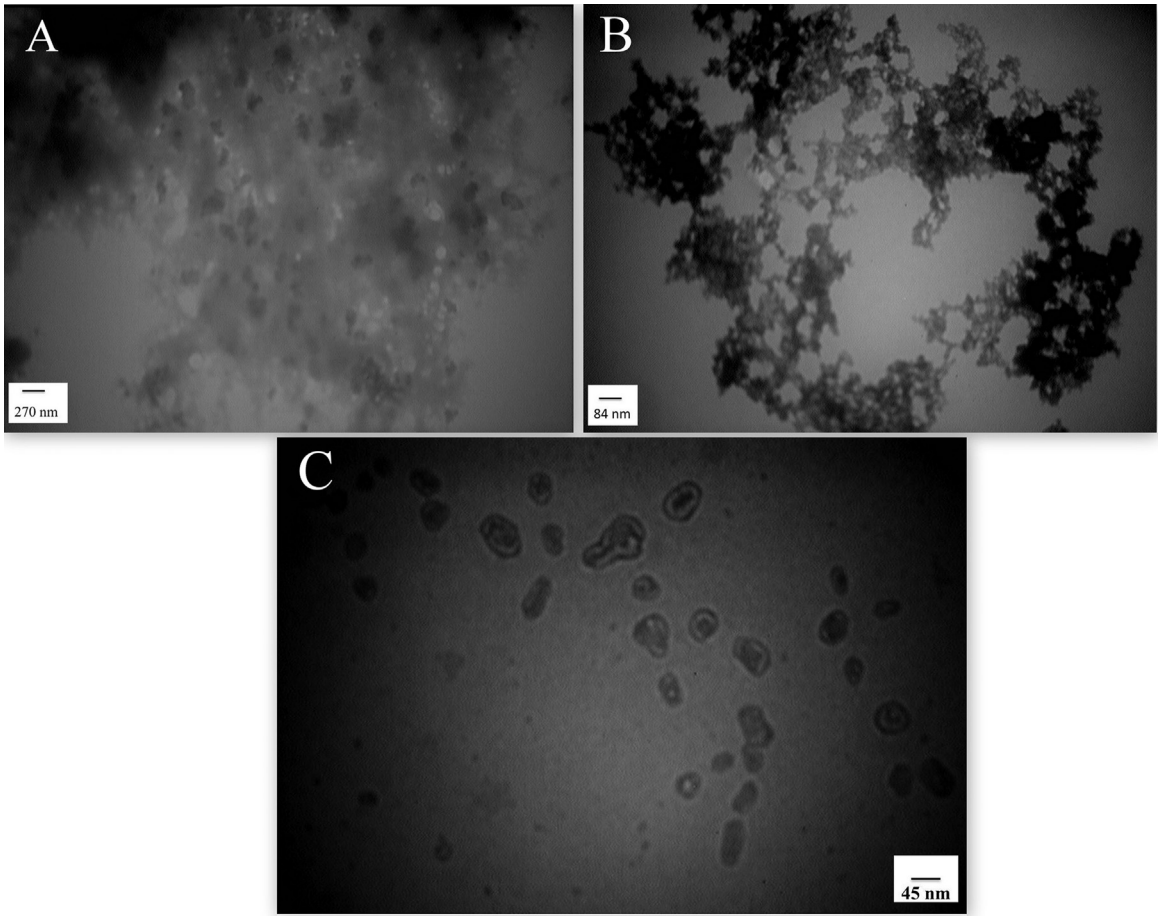

Fig. 6. TEM micrographs of complexes prepared by solvent diffusion method. PS (A), PS/pEGFP-p53 (B), PSCFO/pEGFP-p53 (C).

nanoparticles due to the presence of the organic components. The D_m was smaller than the particle size observed from TEM measurement which was most likely due to contributions of a magnetically "dead layer" reported to be present on the surface of particles [41].

3.4. Transmission electron microscopic studies

The morphology, structure, and size properties of iron oleate, PSCFO, PS, PS/pEGFP-p53 and PSCFO/pEGFP-p53 were examined by TEM.

Nanoparticles size measurements were processed using Image J software. The average diameter of iron oleate nanoparticles was 34 ± 12 nm ($\delta = 35\%$). Fe_3O_4 nanoparticles were coated with oleic acid as capping agent, rendering them well-separated and stable in non-polar solvents, they maintained their original cubic shape with a good monodispersity (Fig. 5(A)). Iron oleate nanoparticles that were coated by PS using microemulation method gave rise to core–shell nanoparticles with a diameter of 100 ± 50 nm ($\delta = 50\%$). Prepared nanocomposites were quite homogeneous in size, separated and single-cored (Fig. 5(B and C)). However, some multi-core nanoparticles fused together, but this was relatively uncommon.

Macroscopically, PS particles appeared as a long chain of interacting particles composed of small nanoparticles with a calculated diameter of 166 ± 25 nm ($\delta = 15\%$) (Fig. 6(A)). Loading of pEGFP-p53 on the PS (175 ± 17 nm, $\delta = 10\%$) nanoparticles resulted in their appearing as long chain of interacting particles (Fig. 6(B)). PSCFO/pEGFP-p53 (172 ± 3 nm, $\delta = 2\%$) nanoparticles resulted in separated and single-cored (Fig. 6(C)).

The iron oleate had a highly porous structure as a result of the topotactic transformation of goethite (FeOOH) to magnetite (Fe_3O_4), which induced the formation of slit-shaped micropores via the removal of water droplets generated during the reaction process. Spherical monodispersed particles of 34 nm diameter that were prepared had a narrow size distribution, indicating the particles were monodispersed. Using iron oleate as precursor in octadecence resulted in small monodispersed spherical particles [42]. A slight aggregation can be observed which was due to the aggregation of individual particles with an incomplete coating by oleic acid molecules [43]. At 1–100 nm length scales, Brownian motion leads to nanoparticle aggregation resulting in 'local aggregates' of typical size 0.1–10 μm [44]. Iron oleate nanoparticles were coated by pullulan–spermine to give rise to core–shell nanoparticles. Prepared nanocomposites were quite homogeneous in size, separated and single-cored (Fig. 5(B and C)). A polymer shell allows dispersion of superparamagnetic iron oxide nanoparticles in aqueous medium, but it could also allow for reversible aggregation and dispersion [45]. PSCFO nanoparticles were nearly spherical in shape and well-separated, but there was no significant change in size resulting from the PS coating process, as shown in Fig. 5 (B and C).

3.5. Dynamic light scattering (DLS)

Hydrodynamic size readings of the synthesized nanoparticles as determined by DLS are even more significant than values obtained by TEM for nanoparticles functionalized with long-chained ligands. A mean hydrodynamic size value for iron oleate was 177 ± 18.3 nm ($\delta = 10.3\%$) versus 80.5 ± 18.5 nm ($\delta = 23\%$) for PSCFO. Nanoparticles with hydrodynamic size more than 200 nm

Fig. 7. Gel retardation assay (agarose, 1%) of free EGFP-p53 plasmid (lanes 1–3), PSCFO/pEGFP-p53 (lanes 4–6) and PS/pEGFP-p53 (lanes 7–9) (triplicate runs of the same samples).

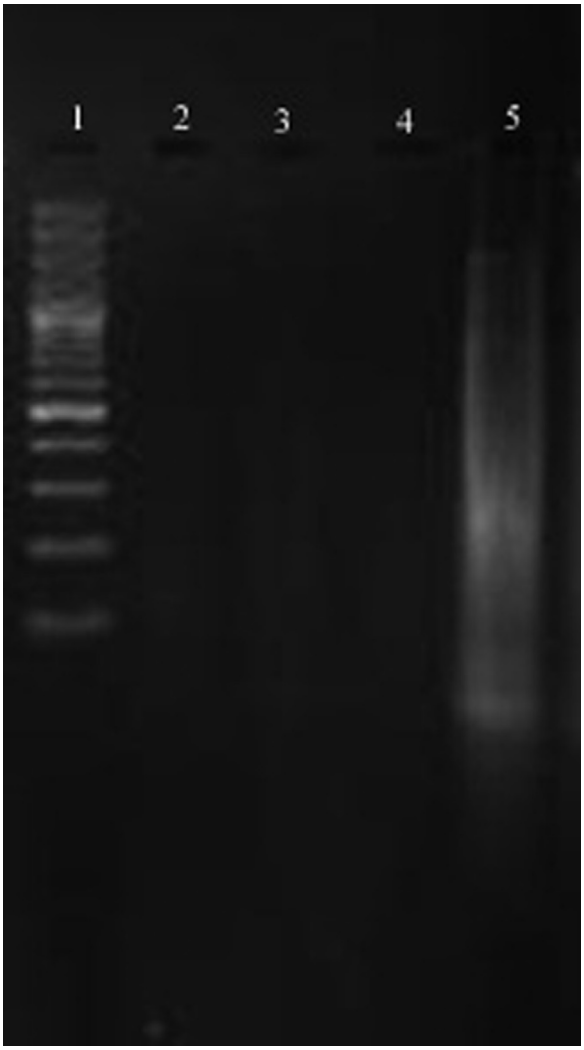

Fig. 8. Agarose gel electrophoresis of the DNA captured on nanoparticles. DNA marker (1), DNase I digested PSCFO (positive control) (2), DNase I digested PSCFO/pEGFP-p53 (3), DNase I digested PS/pEGFP-p53 (4), DNase I digested naked pEGFP-p53 (negative control) (5).

were not included in average size calculations as these were probably multicore nanocomposites. An average hydrodynamic size of 200 ± 21 nm ($\delta = 10.3\%$) was shown for PS particles. At the same time, pEGFP-p53 loaded on PS and PSCFO showed a mean hydrodynamic size of 120 ± 43 nm ($\delta = 36\%$) and 179 ± 15 nm ($\delta = 10\%$), respectively.

The average diameters determined by DLS were larger than the sizes determined from the TEM images for the corresponding samples. This was presumably because DLS gave the mean hydrodynamic diameter of the magnetite core surrounded by the organic and solvation layers, whereas TEM gave the diameter of magnetic nanoparticles alone in the dry state [46].

3.6. Colloidal stability

Colloidal stability of the nanoparticles plays a very significant role in relation to in vivo biomedical applications. Nanoparticle zeta-potential at pH 7.4 was -37 ± 6 mV for iron oleate, -70 ± 26 mV for PS particles, -70 ± 26 mV for PSCFO, -69 ± 15 mV for pEGFP-p53 loaded on PS and -43 ± 8 mV for pEGFP-p53 loaded on the PSCFO. Compared to uncoated magnetite nanoparticles, pullulan–spermine coated particles were more stable at the physiological pH of 7.4, reflecting the advantage of such coating for nanoparticle stabilization.

3.7. Gel retardation assay

Fig. 7 shows the migration of the free plasmid (lanes 1–3) and the PSCFO/pEGFP-p53 and PS/pEGFP-p53 nanoparticles (lanes 4–9). PSCFO/pEGFP-p53 and PS/pEGFP-p53 nanoparticles did not display a strong fluorescence. The smear band observed in lanes 7–9 suggested that a release of DNA might have occurred during electrophoresis. A similar smearing was not observed in lanes 4–6, leading to the hypothesis that strong electrostatic interactions exist between PSCFO and pEGFP-p53, at least under the experimental conditions used.

3.8. Ethidium bromide intercalation assay

The degree of DNA condensation was determined as a function of the *N*/*P* ratio by an EtBr displacement assay. The incorporation of DNA into PSCFO/pEGFP-p53 and PS/pEGFP-p53 nanoparticles was monitored by following the fluorescence emission of EtBr intercalated into the DNA double helix. The results showed that PSCFO and PS were able to achieve nearly complete quenching (FI% = 18 and 0, respectively), indicating complete binding between PSCFO and PS and pEGFP-p53.

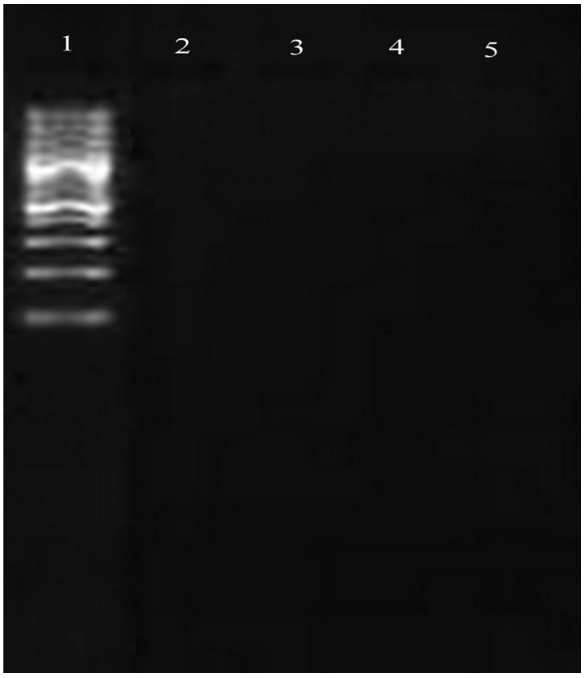

Fig. 9. Agarose gel electrophoresis of the nanoparticles encapsulating DNA. DNA marker (1), PSCFO/pEGFP-p53 in serum-free medium (2), PSCFO/pEGFP-p53 in PBS (3), PS/pEGFP-p53 in serum-free medium (4), PS/pEGFP-p53 in PBS (5).

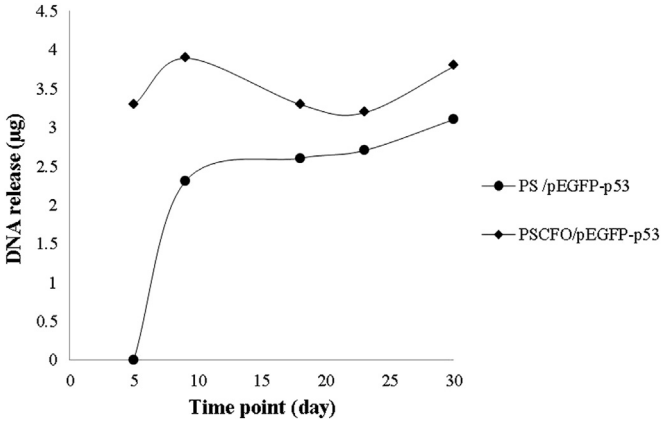

Fig. 10. DNA release from the PSCFO/pEGFP-p53 and PS/pEGFP-p53 systems as determined by spectrophotometry.

3.9. Trypan blue assay

The slight quenching effect induced by trypan blue suggested that most of the loaded DNA had been encapsulated inside the nanoparticles.

3.10. Electrophoretic nuclease resistance and stability assays

The ability of the copolymer to entrap the plasmid was studied using the agarose electrophoresis technique. Following agarose gel electrophoresis, Fig. 8 (lanes 3 and 4), no migration of free DNA was observed, indicating that most of the DNA was captured by the nanoparticles because of the high affinity of PS for the DNA [47,48]. Indeed, it is known that a strong electrostatic interaction exists between the phosphate groups of DNA and the amino groups of PS, as well as hydrophobic and hydrogen bonds.

The stability of PSCFO/pEGFP-p53 and PS/pEGFP-p53 complexes (7%) was evaluated at 7 days in the serum-free medium and in the absence of medium (PBS) (Fig. 9). The fluorescence intensity of bands corresponding to DNA and their electrophoretic mobility were observed and compared with those obtained with naked DNA. The fluorescence band was not localized in the well containing the nanocomplexes, suggesting that the absence of DNA binding to the surface of the nanoparticle. Moreover, no smear bands were observed in lanes 2–5, suggesting that a release of DNA would not have occurred during electrophoresis. Nanoparticle stability and nucleic acid protection are important parameters for efficient nucleic acid delivery [49]. The results indicated that the nanoparticles complexes were able to protect DNA at supra physiological concentration of nuclease. Nuclease protection is of great importance for gene delivery systems through maintenance of cargo bioavailability and improved pharmacokinetic profile, thereby increasing the therapeutic potential of these nanoparticles.

3.11. DNA release studies

DNA release from the constructed systems was analyzed by spectrophotometry. At fixed time points of 5, 9, 18, 23, and 30 days the supernatant was collected and the kinetics of DNA release from PSCFO/pEGFP-p53 and PS/pEGFP-p53 complexes were measured (Fig. 10). The release of DNA from PSCFO/pEGFP-p53 nanoparticles showed an initial release within the first 5 days and continued during 9 days of incubation. Thereafter, the rate of release declined until the 23rd day. A slight increase in DNA release was observed on day 30. No DNA release was observed from PS/pEGFP-p53 nanoparticles in the first five days. From day 9, the release of DNA from the nanoparticle complex was observed until the 30th day, yielding more than 25 μg of the encapsulated DNA.

3.12. Cytotoxicity assay

The cytotoxicity of various concentrations of nanoparticles prepared in this study was evaluated after 24 h incubation of the trypsinized U87 cells with the transfection complexes. The results showed that as the concentration of PSCFO/pEGFP-p53 rose from zero to 500 μg/μl on the basis of the initial concentration, the survival rate of the U87 cells decreased. Both the primary effect of the nanoparticles or their side effects could be responsible for the observed cytotoxicity [50]. The broad spectrum of different nanoparticles–cell interactions include an impact of nanoparticles on the plasma membrane, nanoparticle-mediated intracellular trafficking, and nanoparticle-dependent perturbation of basic cellular functions [51]. Therefore, a balance between cell membrane integrity and cytotoxicity of the therapeutic agent is a crucial aspect in gene delivery. The survival rate with regard to cytotoxicity was 92% at 50 μg PSCFO/pEGFP-p53, with an IC_{50} value of 189 μg/μl, a level similar to that reported previously [38].

4. Conclusion

Magnetic (PSCFO) and nonmagnetic (PS) nanoparticles were fabricated by thermal decomposition and solvent diffusion methods respectively. PSCFO nanoparticles were spherical in morphology and 100 nm in mean diameter, with a unimodal size distribution. The saturated magnetization of the iron oleate and PSCFO nanoparticles reached 14 and 9 emu/g respectively, and they showed superparamagnetic behavior at room temperature. PSCFO nanoparticles displayed magnetite content and good biocompatibility. Hence, the new nanoparticles described here can be developed for therapeutic applications in targeting tumors.

Acknowledgment

The work was part of Ph.D. thesis which has been kindly supported by the Kerman University of Medical Sciences (KMU) of Iran.

References

[1] M. Olivo, R. Bhuvaneswari, N. Dendukuri, P.S.-P. Thong, Targeted therapy of cancer using photodynamic therapy in combination with multi-faceted anti-tumor modalities, Pharmaceuticals 3 (2010) 1507–1529.
[2] G. Caruso, M. Caffo, C. Alafaci, G. Raudino, D. Cafarella, S. Lucerna, F. M. Salpietro, F. Tomasello, Could nanoparticle systems have a role in the treatment of cerebral gliomas? Nanomed.: Nanotechnol. Biol. Med. 7 (2011) 744–752.
[3] W.J. He, H. Hosseinkhani, P.D. Hong, C.H. Chiang, D.S. Yu, Magnetic nanoparticles for imaging technology, Int. J. Nanotechnol. 10 (2013) 930–944.
[4] C.A. Charitidis, P. Georgiou, M.A. Koklioti, A.-F. Trompeta, V. Markakis, Manufacturing nanomaterials: from research to industry, Manuf. Rev. 1 (2014) 11.
[5] Â.L. Andrade, M.A. Valente, J.M.F. Ferreira, J.D. Fabris, Preparation of size-controlled nanoparticles of magnetite, J. Magn. Magn. Mater. 324 (2012) 1753–1757.
[6] M. Willard, L. Kurihara, E. Carpenter, S. Calvin, V. Harris, Chemically prepared magnetic nanoparticles, Int. Mater. Rev. 49 (2004) 125–170.
[7] C. Sun, D. Xue, Crystallization of nanomaterials, Curr. Opin. Chem. Eng. 1 (2012) 108–116.
[8] T.K. Sau, A.L. Rogach, Nonspherical noble metal nanoparticles: colloid-chemical synthesis and morphology control, Adv. Mater. 22 (2010) 1781–1804.
[9] H. Guo, A.S. Barnard, Naturally occurring iron oxide nanoparticles: morphology, surface chemistry and environmental stability, J. Mater. Chem. A 1 (2013) 27–42.
[10] W.-F. Ma, Y. Zhang, L.-L. Li, L.-J. You, P. Zhang, Y.-T. Zhang, J.-M. Li, M. Yu, J. Guo, H.-J. Lu, Tailor-made magnetic Fe3O4@ mTiO2 microspheres with a tunable mesoporous anatase shell for highly selective and effective enrichment of phosphopeptides, ACS Nano 6 (2012) 3179–3188.
[11] N. Tran, T.J. Webster, Magnetic nanoparticles: biomedical applications and challenges, J. Mater. Chem. 20 (2010) 8760–8767.
[12] P. Brown, C.P. Butts, J. Cheng, J. Eastoe, C.A. Russell, G.N. Smith, Magnetic emulsions with responsive surfactants, Soft Matter 8 (2012) 7545–7546.
[13] M. Gharagozlou, Study on the influence of annealing temperature and ferrite content on the structural and magnetic properties of $x\,(NiFe_2O_4)/(100-x)\,SiO_2$ nanocomposites, J. Alloy. Compd. 495 (2010) 217–223.
[14] A. Pathak, S.P. Vyas, K.C. Gupta, Nano-vectors for efficient liver specific gene transfer, Int. J. Nanomed. 3 (2008) 31.
[15] L. Jin, X. Zeng, M. Liu, Y. Deng, N. He, Current progress in gene delivery technology based on chemical methods and nano-carriers, Theranostics 4 (2014) 240.
[16] L.B. Thomsen, J. Lichota, K.S. Kim, T. Moos, Gene delivery by pullulan derivatives in brain capillary endothelial cells for protein secretion, J. Control. Release 151 (2011) 45–50.
[17] H. Hosseinkhani, F. Abedini, K.L. Ou, A.J. Domb, Polymers in gene therapy technology, Polym. Adv. Technol. 26 (2015) 198–211.
[18] D.K. Thakor, Y.D. Teng, H. Obata, K. Nagane, S. Saito, Y. Tabata, Nontoxic genetic engineering of mesenchymal stem cells using serum-compatible pullulan-spermine/DNA anioplexes, Tissue Eng. C: Methods 17 (2010) 131–144.
[19] B. Vogelstein, K.W. Kinzler, Cancer genes and the pathways they control, Nat. Med. 10 (2004) 789–799.
[20] A.M. Soto, C. Sonnenschein, The somatic mutation theory of cancer: growing problems with the paradigm? Bioessays 26 (2004) 1097–1107.
[21] A.M. Oliveira, J.S. Ross, J.A. Fletcher, Tumor Suppressor genes in breast cancer the gatekeepers and the caretakers, Am. J. Clin. Pathol. Pathol. Patterns Rev. 124 (2005) S16–S28.
[22] P.A. Futreal, L. Coin, M. Marshall, T. Down, T. Hubbard, R. Wooster, N. Rahman, M.R. Stratton, A census of human cancer genes, Nat. Rev. Cancer 4 (2004) 177–183.
[23] A. Vazquez, E.E. Bond, A.J. Levine, G.L. Bond, The genetics of the p53 pathway, apoptosis and cancer therapy, Nat. Rev. Drug Discov. 7 (2008) 979–987.
[24] L.T. Vassilev, B.T. Vu, B. Graves, D. Carvajal, F. Podlaski, Z. Filipovic, N. Kong, U. Kammlott, C. Lukacs, C. Klein, In vivo activation of the p53 pathway by small-molecule antagonists of MDM2, Sci. Signal. 303 (2004) 844–848.
[25] D. Seecharan, F. Farassati, A. Pollack, Innovativevative surgical management of glioma, in: F. Farassati (Ed.), Novel Therapeutic Concepts in Targeting Glioma, InTech, University Campus STeP Ri, Croatia,, 2012, pp. 306.
[26] S.D. Boyd, K.Y. Tsai, T. Jacks, An intact HDM2 RING-finger domain is required for nuclear exclusion of p53, Nat. Cell Biol. 2 (2000) 563–568.
[27] W.Y. William, J.C. Falkner, C.T. Yavuz, V.L. Colvin, Synthesis of monodisperse iron oxide nanocrystals by thermal decomposition of iron carboxylate salts, Chem. Commun. (2004) 2306–2307.
[28] G. Hermansson Bioconjugate Techniques, 2nd ed., 2008, Elsevier Academic Press; Amsterdam; Boston.
[29] O. Taratula, O. Garbuzenko, R. Savla, Y. Andrew Wang, H. He, T. Minko, Multifunctional nanomedicine platform for cancer specific delivery of siRNA by superparamagnetic iron oxide nanoparticles-dendrimer complexes, Curr. Drug Deliv. 8 (2011) 59–69.
[30] A. Masotti, F. Marino, G. Ortaggi, C. Palocci, Fluorescence and scanning electron microscopy of chitosan/DNA nanoparticles for biological applications, in: A. Mendes-Vilas, J. Diaz (Eds.), Modern Research and Educational Topics in Microscopy., 2007, pp. 690–696.
[31] Z. Mahdinia, R. Eftekharvaghefi, F. Nabipour, In vitro inhibition of the growth of glioblastoma by Teucrium polium crude extract and fractions, Int. J. Phytomed. 4 (2013) 582–588.
[32] W. Wu, Z. Wu, T. Yu, C. Jiang, W.-S. Kim, Recent progress on magnetic iron oxide nanoparticles: synthesis, surface functional strategies and biomedical applications, Sci. Technol. Adv. Mater. 16 (2015) 23501.
[33] C.J. Chen, H.Y. Lai, C.C. Lin, J.S. Wang, R.K. Chiang, Preparation of monodisperse iron oxide nanoparticles via the synthesis and decomposition of iron fatty acid complexes, Nanoscale Res. Lett. 4 (2009) 1343–1350.
[34] A.D. Abid, M. Kanematsu, T.M. Young, I.M. Kennedy, Arsenic removal from water using flame-synthesized iron oxide nanoparticles with variable oxidation states, Aerosol Sci. Technol. 47 (2013) 169–176.
[35] B. Faure, G. Salazar-Alvarez, A. Ahniyaz, I. Villaluenga, G. Berriozabal, Y.R. D. Miguel, L. Bergström, Dispersion and surface functionalization of oxide nanoparticles for transparent photocatalytic and UV-protecting coatings and sunscreens, Sci. Technol. Adv. Mater. 14 (2013) 23001.
[36] S. Kango, S. Kalia, A. Celli, J. Njuguna, Y. Habibi, R. Kumar, Surface modification of inorganic nanoparticles for development of organic-inorganic nanocomposites – a review, Prog. Polym. Sci. 38 (2013) 1232–1261.
[37] E.V. Shtykova, X. Huang, X. Gao, J.C. Dyke, A.L. Schmucker, B. Dragnea, N. Remmes, D.V. Baxter, B. Stein, P.V. Konarev, Hydrophilic monodisperse magnetic nanoparticles protected by an amphiphilic alternating copolymer, J. Phys. Chem. C 112 (2008) 16809–16817.
[38] F. Gao, Y. Cai, J. Zhou, X. Xie, W. Ouyang, Y. Zhang, X. Wang, X. Zhang, X. Wang, L. Zhao, J. Tang, Pullulan acetate coated magnetite nanoparticles for hyperthermia: preparation, characterization and in vitro experiments, Nano Res. 3 (2010) 23–31.
[39] A.M. Prodan, S.L. Iconaru, C.M. Chifiriuc, C. Bleotu, C.S. Ciobanu, M. Motelica-Heino, S. Sizaret, D. Predoi, Magnetic properties and biological activity evaluation of iron oxide nanoparticles, J. Nanomater. 2013 (2013) 7.
[40] C. Passow, B. Fischer, M. Sprung, M. Köckerling, J. Wagner, Direction-dependent freezing of diamagnetic colloidal tracers suspended in paramagnetic ionic liquids, Langmuir 30 (2014) 7283–7288.
[41] Z. Khayat Sarkar, F. Khayat Sarkar, Magnetic iron oxide nanoparticles, polyethylene glycol, surfactant, superparamagnetic, chemical co-precipitation, Int. J. Nanosci. Nanotechnol. 7 (2011) 197–200.
[42] R. Hufschmid, H. Arami, R.M. Ferguson, M. Gonzales, E. Teeman, L.N. Brush, N. D. Browning, K.M. Krishnan, Synthesis of phase-pure and monodisperse iron oxide nanoparticles by thermal decomposition, Nanoscale 7 (2015) 11142–11154.
[43] M. Mahdavi, M.B. Ahmad, M.J. Haron, F. Namvar, B. Nadi, M.Z. Rahman, J. Amin, Synthesis, surface modification and characterisation of biocompatible magnetic iron oxide nanoparticles for biomedical applications, Molecules 18 (2013) 7533–7548.
[44] G. Pranami, Understanding Nanoparticle Aggregation, 2009.
[45] S. Kurzhals, R. Zirbs, E. Reimhult, Synthesis and magneto-thermal actuation of iron oxide CorePNIPAM shell nanoparticles, ACS Appl. Mater. Interfaces 7 (2015) 19342–19352.
[46] J. Tuoriniemi, A.-C.J.H. Johnsson, J.P. Holmberg, S. Gustafsson, J.A. Gallego-Urrea, E. Olsson, J.B.C. Pettersson, M. Hassellöv, Intermethod comparison of the particle size distributions of colloidal silica nanoparticles, Sci. Technol. Adv. Mater. 15 (2014) 35009-19.
[47] M. Alameh, D. DeJesus, M. Jean, V. Darras, M. Thibault, M. Lavertu, M. D. Buschmann, A. Merzouki, Low molecular weight chitosan nanoparticulate system at low *N*:*P* ratio for nontoxic polynucleotide delivery, Int. J. Nanomed. 7 (2012) 1399–1414.
[48] M. Jean, M. Alameh, D. De Jesus, M. Thibault, M. Lavertu, V. Darras, M. Nelea, M.D. Buschmann, A. Merzouki, Chitosan-based therapeutic nanoparticles for combination gene therapy and gene silencing of in vitro cell lines relevant to type 2 diabetes, Eur. J. Pharm. Sci. 45 (2012) 138–149.
[49] M. Kapoor, D.J. Burgess, Targeted delivery of nucleic acid therapeutics via nonviral vectors, in:P.V. Devarajan, S.Jain (Eds.), Targeted Drug Delivery: Concepts and Design, Springer, 2015, pp. 271–312.
[50] A. Panariti, G. Miserocchi, I. Rivolta, The effect of nanoparticle uptake on cellular behavior: disrupting or enabling functions? Nanotechnol. Sci. Appl. 5 (2012) 87–100.
[51] J. Lojk, V.B. Bregar, M. Rajh, K. Mis, M.E. Kreft, S. Pirkmajer, P. Veranic, M. Pavlin, Cell type-specific response to high intracellular loading of polyacrylic acid-coated magnetic nanoparticles, Int. J. Nanomed 10 (2015) 1449–1462.